Discerning the magnetization reversal mechanism and magnetic interactions in arrays of FeNi nanowires

Alonso J. Campos-Hernández, Ester M. Palmero, Alberto Bollero

Discerning the magnetization reversal mechanism and magnetic interactions in arrays of FeNi nanowires

Alonso J. Campos-Hernández, Ester M. Palmero* and Alberto Bollero[§]

Group of Permanent Magnets and Applications, IMDEA Nanoscience, 28049 Madrid, Spain

*Corresponding author (E.M. Palmero) - Email: ester.palmero@imdea.org

Abstract

FeNi nanowires (NWs), 40 nm in diameter, were grown by electrodeposition. Compositional analysis showed Fe anomalous co-deposition, with different trends across the different potentials and electrolytes used. Those trends were explained within a modified Bocris-Drazic-Despic chemical reactions model, highlighting the importance of the electrochemical theory in understanding Fe-Ni electrodeposited systems. Structural characterization showed a change from a body-centred cubic structure for Fe-rich NWs to face-centred cubic at mid and low Fe content. Magnetic hysteresis measurements showed a range of coercivities from 20 mT for Fe-rich to 100 mT for Ni-rich NWs. Angular measurements allowed to determine that the magnetization reversal mechanism was dominated by transverse domain wall reversal. The analysis also hinted at the non-shape anisotropy acting as a demagnetizing force. First-order reversal curves (FORCs) showed that arrays with a high absolute value for the non-shape anisotropy had higher magnetic interactions, and vice versa. The non-shape anisotropy is dominated by the magnetostatic interactions between NWs, causing a weakening of the magnetic hardness. In combination with the coercivity angular measurements, the FORC analysis explained the shift in easy axis preference depending on NW chemical composition observed in the samples' hysteresis loops.

Keywords

FeNi, nanowires, electrochemistry, magnetization reversal, magnetic interactions

1. Introduction

The synthesis and study of nanowires (NWs) has gathered increased attention lately due to their promising future as next-generation magnetic memories [1], [2], [3], [4], nano-sensors [5], [6], [7], [8] and components of foldable electronic devices [9], [10], [11], [12], [13], among other applications. The different synthesis methods and the high number of degrees of freedom in the synthesis of arrays of NWs permits greatly tuned compositions, structures and, consequently,

[§]Present address (A. Bollero): Advanced Technologies and Micro Systems, Robert Bosch GmbH, Corporate Sector Research, Renningen, 70465 Stuttgart, Germany
Email: Alberto.Bollero@de.bosch.com

magnetic properties. In particular, electrodeposited FeNi NWs are promising as they can be made of well-known alloys with useful magnetic properties for technological applications (e.g., $Fe_{20}Ni_{80}$, known as "permalloy"), and are currently being investigated for applications such as race-track magnetic memories [14], [15], [16], [17] by exploiting the range of properties of the FeNi alloys at different compositions.

However, the electrochemical synthesis of FeNi NWs poses the issue of Fe anomalous co-deposition, by which Fe deposits in the NWs in greater amounts than it is present in the electrolyte. The Fe selectivity caused by this effect, defined as the ratio of Fe fraction in the sample to the Fe fraction in the electrolyte, has been observed to change by a great number of factors such as electrodeposition potential [18], [19], [20], nanowires geometry [18], [19], [21]; electrolyte composition [18], [21], [22], [23]; period used in pulsed electrodeposition [24], etc.

These observations typically lack a theoretical analysis of the anomalous co-deposition phenomenon, which hinders the capacity to predict the changes in Fe selectivity to be expected under different synthesis conditions. Therefore, the consistent application of anomalous co-deposition models to measured compositional data is of great interest to the academic community, especially given that the more magnetism- and materials- oriented side of the community scarcely focuses on the pure electrochemical aspects of this problem.

Additionally, it is crucial to investigate the magnetic properties of the NW samples in an integrated manner, not only making use of different experimental techniques but also analysing their results jointly as part of a broader analysis. NW magnetic properties can vary depending on multiple factors, such as NW diameter [25], [26], [27], chemical composition [26], [27], [28], [29], [30], [31], [32], structural modulation [33], [34], [35], [36], etc. Therefore, investigating the change in the magnetic properties with the different NW characteristics using an integrated approach in the experimental design and data analysis would be highly useful.

Thus, in this work we present a study of the correlation between the composition, crystallographic phases and magnetic properties of electrodeposited arrays of FeNi NWs synthesized under a range of electrochemical potentials and electrolyte compositions. The observed changes in the sample chemical composition caused by the anomalous co-deposition phenomenon were analysed under a modified Bocris-Drazic-Despic (BDD) model [38] to better explain at the chemical level the trends observed in Fe selectivity. The changes in the magnetic interactions among NWs in the array depending on the NWs composition were also analysed via coercivity angular measurements and first-order reversal curves (FORCs).

To our knowledge, this is the first study on FeNi NWs where angular coercivity measurements and FORC diagrams are jointly analysed to thoroughly study the magnetic properties of the NWs such as their magnetostatic interactions and their impact on secondary magnetic properties such

as hysteresis loop shape and easy axis direction preference. Additionally, the analysis of the Fe anomalous co-deposition trends observed through the BDD model discussed later on is crucial in both calling the attention of materials scientists working solely on the magnetism of metallic NWs to the electrochemical aspects of the research, as well as in aiding future works in predicting their own Fe-Ni compositions trends despite the anomalous co-deposition effect. Overall, our findings emphasize the importance of the control of the multiple degrees of freedom in the synthesis of NWs (electrolyte composition, electrodeposition potential and mode, etc.) in tailoring the properties of FeNi NWs.

2. Experimental methods

The arrays of FeNi NWs were prepared by electrochemical potentiostatic deposition into the hexagonally self-assembled pores of anodized aluminum oxide (AAO) templates. The AAO templates were prepared from Al foils of 99.999% purity by a two-steps anodization method [39], [40], [41]. These pores showed a mean diameter of 40 nm, and a mean inter-pore distance of 105 nm (Fig. 1a). After the anodization steps, the back-side aluminum layer and the alumina layer at the bottom of the pores were selective chemically etched. An electrical contact made of Au at one side of the membrane was grown to act as work electrode in the synthesis of the FeNi NWs by electrodeposition.

The FeNi NWs were then grown into the alumina nanopores by potentiostatic electrodeposition in a three-electrodes electrochemical cell configuration using aqueous electrolytes with the following composition: $FeSO_4 \cdot 7H_2O$ ranging between 0.06 and 0.19 M, $NiCl_2 \cdot 6H_2O$ in the range of 0.07 and 0.20 M, and 0.01 M of ascorbic acid. The composition of the electrolytes was tuned to end with electrolytes containing 23, 50 and 75% of Fe solute concentration. A platinum mesh was used as the counter electrode, and the electrodeposition potential was varied in the range between -1.1 and -3.0 V vs the reference Ag/AgCl electrode, except for the arrays of pure-Fe and pure-Ni NWs which were grown at -1.1 V. Both samples were prepared using aqueous electrolytes, containing 0.22 M of $FeSO_4 \cdot 7H_2O$ for the Fe NWs, and 0.84 M of $NiCl_2 \cdot 6H_2O$ with 0.15 M of $NiSO_4 \cdot 6H_2O$ for the Ni NWs. In both cases 0.16 M of boric acid was used, while for the Fe NWs sample 0.06 M of L-ascorbic acid was also used. The NWs diameter was determined to be around 40 nm (see Fig. 1c), with the NWs having been released from the AAO template by the application of phosphoric acid solution to dissolve it. NWs with an apparently larger diameter in Fig. 1c are the result of the overlapping of several NWs.

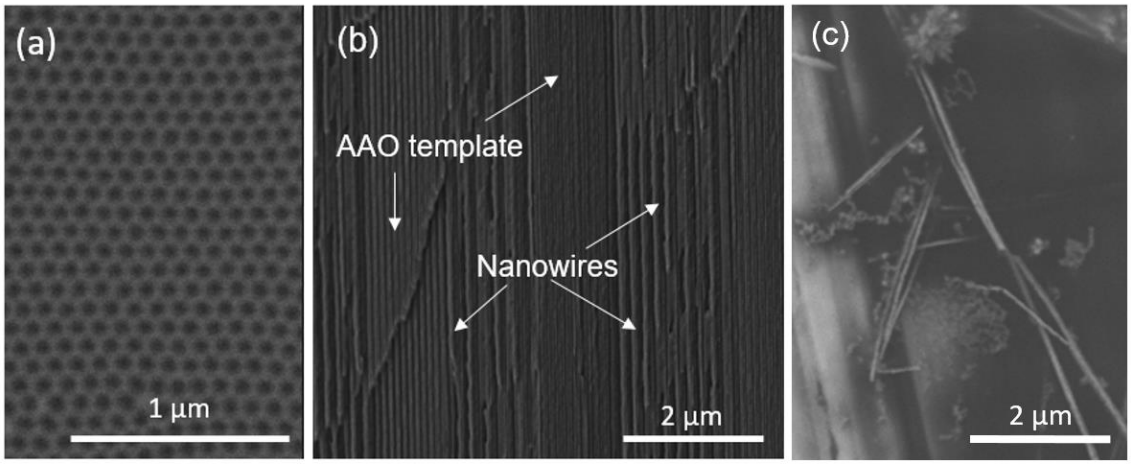

Figure 1. *(a) Top view and (b) cross section SEM images of the anodized aluminum oxide (AAO) membrane showing the top side of the nanopores and a representative array of FeNi NWs, respectively. (c) NWs released from the membrane and dispersed on a flat surface.*

Morphological characterization was carried out using a Scanning Electron Microscope (SEM), model Zeiss UHR SEM Auriga. Energy-dispersive X-ray spectroscopy (EDS/EDX) chemical composition analysis of the samples was done using a Bruker Quantax EDX, XFlash 6I30 model, attached to a Hitachi S-3000N SEM. These EDX measurements were taken from a cross-sectional view of the NW arrays (see Fig. 1b) in order to include as many NWs as possible in the measurement and therefore minimize the measurement error. The crystallographic structure of the NWs was performed by X-ray diffraction (XRD) using a Rigaku Smartlab SE diffractometer in Bragg-Brentano configuration with Cu-K_α radiation ($\lambda = 0.1541$ nm). The magnetic measurements were done using a Lake Shore 7400 series Vibrating Sample Magnetometer (VSM) by applying the magnetic field with an angle, θ, to the nanowire longitudinal axis. Data processing to obtain the FORC diagrams was carried out using the FORCinel software package [42].

3. Results and discussion

3.1 Compositional analysis

The arrays of FeNi NWs synthesized using the different electrolytes within the analysed range of electrodeposition potentials were measured by EDX to determine their composition (see raw EDX spectra of selected samples in Fig. 1 of the Supplementary Material). After calculating sample compositions, all electrolyte composition showed the anomalous co-deposition phenomenon, by which Fe is deposited in a higher concentration than it is present in the electrolyte. The electrodeposition potential range in which the phenomenon occurred, as well as the Fe selectivity (the ratio of Fe content in the FeNi NWs to the content in the electrolyte), were dependant on the electrolyte concentration. It was observed that FeNi NWs synthesized with the lowest Fe concentration electrolyte (i.e., 23% of Fe solute in the electrolyte) had both a wider potential range

in which no anomalous co-deposition occurred (from -1.1 to -2.0 V) as well as a higher selectivity once the anomalous co-deposition mode began (i.e., increased difference among the Fe content in the NWs in comparison to the Fe content in the electrolyte as can be observed in Fig. 2).

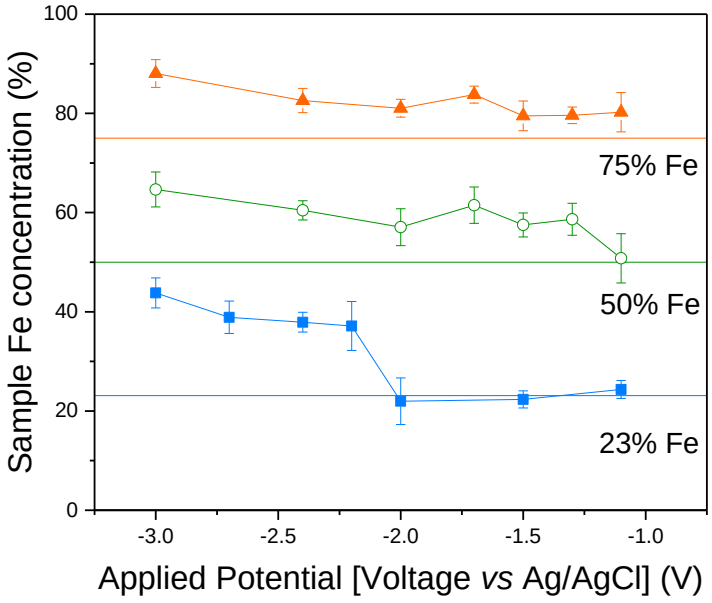

Figure 2. *Evolution of the Fe concentration in the FeNi NWs as a function of the electrodeposition potential for different electrolyte Fe concentrations. As a reference, horizontal lines have been plotted for the Fe content in the different electrolytes.*

These experimental results were analysed under the framework of a modified Bocris-Drazic-Despic (BDD) model [38], presented by Dragos *et al.* to explain the anomalous co-deposition of Fe in FeNi NWs. In this model, the key reaction step of the electrodeposition process occurs between the H^+ in solution and metal hydroxides adsorbed to the electrode surface, MOH^+_{ads} (M = Fe, Ni). MOH^+_{ads} is formed from M^{2+} ions in the solution, and leads to M deposition at the electrode by reduction with an e^-. The key reaction step causing the anomalous co-deposition in this model is

$$H^+ + MOH^+_{ads} \rightarrow H_2O + M^{2+} (M = Fe, Ni) \quad (1),$$

by which the hydroxide ions are desorbed and return to the solution as free metal ions. The much higher dissociation constants of the Ni hydroxide compared to the Fe one (approximately 1,000 times higher [43], [44]) means that more Ni is returned to the solution as Ni^{2+} than Fe is as Fe^{2+}, so that more Ni is removed from the adsorbed state where it can be deposited, leading to a relative increase in the deposition of Fe atoms. This increase in Fe selectivity (the ratio between the

deposited Fe fraction and the electrolyte Fe fraction) is the phenomenon known as anomalous co-deposition.

In the light of this model, the two trends observed in the synthesized FeNi NWs series (namely, the lower Fe selectivity and the anomalous co-deposition occurring at higher potentials, when higher Fe electrolyte concentrations are used) can be explained. Assuming both the Fe and Ni ions have equal probabilities of being adsorbed to the electrode as hydroxides, then the proportions of adsorbed hydroxide ions would be the same as the proportions for the solution concentrations. However, due to the much lower stability of the $NiOH^{+}_{ads}$ ion [43], [44], some fraction of those ions is desorbed from the electrode and replaced by $FeOH^{+}_{ads}$ ions. The fraction of Ni hydroxide ions that are desorbed remains approximately constant as the concentration of Fe in solution increases (so long as the changes in pH between different Fe concentrations are small, as per the chemical equilibrium in Eq. (1)), but as Fe concentration increases they represent a smaller proportion of the total number of adsorbed hydroxide ions (i.e., both Ni and Fe ions) because the starting proportion of adsorbed Ni ions is smaller. Thus, a smaller amount of Ni hydroxide ions, with respect to the total, is replaced by Fe hydroxide at the electrode as the Fe concentration in the electrolyte increases. This smaller increase in Fe adsorption is paired with a bigger starting Fe adsorption concentration to yield an overall lower Fe selectivity. In our experiments, we have measured pH values of 2.89, 2.99 and 3.11 for the 23, 50 and 75% Fe concentration electrolytes, respectively, so there are only very small increases in pH as more Fe is added to the electrolyte and the above qualitative model can explain the lower selectivity observed. Similarly, the increased potential range in which anomalous co-deposition occurs when increasing Fe concentration can be attributed to the progressive loss of Ni^{2+} ion saturation at the electrode: when there is more Ni in the electrolyte, the desorbed hydroxide ions can be replaced with new ions easily at high potentials (where there is little desorption, which is enhanced by lower electrodeposition potentials), but with less Ni concentration the replacement is harder and so observable anomalous behaviour occurs in a wider potential range.

Samples grown at -1.1 V for each electrolyte (of composition $Fe_{0.24}Ni_{0.76}$, $Fe_{0.51}Ni_{0.49}$ and $Fe_{0.80}Ni_{0.20}$ for 23, 50 and 75% Fe electrolyte concentration, respectively) were chosen for the more in-depth study, since these samples showed the least anomalous co-deposition of each sample series, therefore being the samples with the chemical composition optimized according to the electrolyte composition.

3.2 Structural and crystallographic analysis

Structural analysis of arrays of FeNi NWs (together with reference arrays of pure-Fe and pure-Ni NWs grown under the same electrochemical conditions) using X-ray diffraction (XRD) showed

a mixture of fcc (face-centred cubic) and bcc (body-centred cubic) phases (see Fig. 3) across the samples. Interestingly, the pure-Fe sample clearly showed a fcc structure, characteristic of γ-Fe, instead of the typical low-temperature bcc phase of α-Fe. It is known that NWs diameter changes are enough to alter the NWs crystal structure [26], [45], and from comparison with the 40 nm-diameter bcc Fe nanowires grown by pulsed electrodeposition in [46], we conclude that the same is true for the electrodeposition mode used.

It is interesting to further note that the $Fe_{0.80}Ni_{0.20}$ sample studied here did show a clear bcc phase, with the (2 0 0), (2 1 1) and (2 2 0) reflections being clearly visible independently, while the (1 1 0) diffraction peak overlaps with the position of the fcc (1 1 1) peak. However, given that no other fcc peaks are found, this peak was assigned as the bcc (1 1 0) peak. This suggests that a fraction of Ni content aids in stabilizing the α-Fe structure. On further increases of Ni content, the fcc phase becomes the dominant one instead.

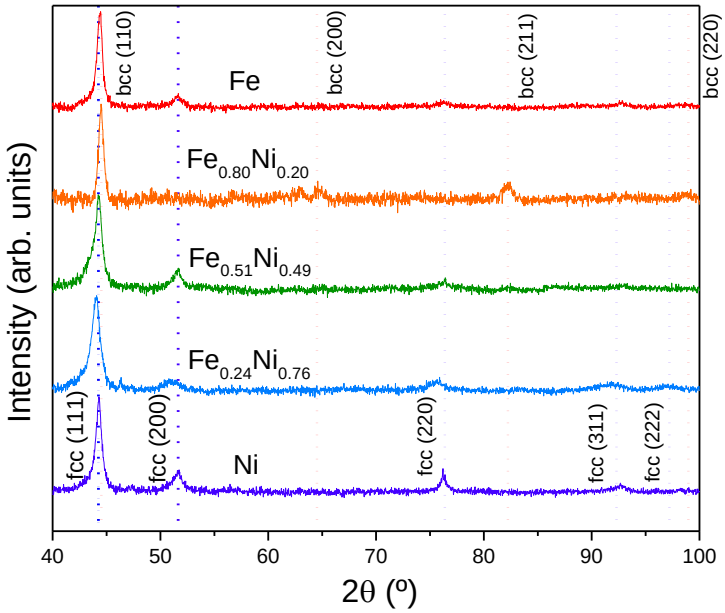

Figure 3. *XRD patterns for the arrays of Fe, Ni and FeNi (with different compositions) NWs synthesized at -1.1 V vs reference electrode (bcc reference peaks are indicated with red dotted lines, and fcc peaks with blue dotted lines).*

3.3 Magnetic characterization

Hysteresis loops were measured for the arrays of FeNi NWs with varying composition under analysis (Fig. 4), to study the magnetization reversal process and correlate it with the composition and crystallographic structure of the NWs. The results showed a very wide range of magnetic behaviours, with the coercivity $\mu_0 H_c$ measured for $\theta = 0^\circ$ ranging from 20 mT for the $Fe_{0.80}Ni_{0.20}$ sample to about 100 mT for the $Fe_{0.24}Ni_{0.76}$ one. Note that, while the hysteresis loops shown are

normalized to their own magnetic moment at saturation, the saturation magnetization for the alloys studied in their bulk form have been considered for the analysis of the obtained results (values included in Table 1 [47]). Additionally, note that some studies [48] have found significant correlation between the nanopore density (of 2.89 10^9 cm^{-2} in our samples) or NW packing fraction (of around 3.6% in our samples) and sample parameters such as the saturation field. In this regard, the saturation field of our Fe sample (56 mT) is in agreement with those reported in [48] for similar packing fractions. However, because packing fractions are equal across all our samples, and instead there is significant variation of chemical composition and its associated physical properties, the investigation of the impact of packing fraction on the properties of our samples was not pursued further.

Fig. 4f shows the evolution of the coercivity $\mu_0 H_c$ and normalized remanence M_r/M_s with Fe content, with the external field applied along the NW axis. The contrast between the high coercivity and remanence values for the Fe, $Fe_{0.24}Ni_{0.76}$ and Ni NWs compared to the $Fe_{0.51}Ni_{0.49}$ and $Fe_{0.80}Ni_{0.20}$ NWs can be explained as the change in the easy axis character of nanowire axis, due to a change in the balance between NW shape anisotropy and NW magnetostatic interactions. Note that this type of coercivity and remanence evolution has been observed previously in other works dealing with Fe-based alloys NWs [26]. As can be seen by comparing the measurements done for $\theta = 0°$ and 90°, for the Fe, $Fe_{0.24}Ni_{0.76}$, and Ni arrays for $\theta = 0°$ ($\theta = 90°$) the nanowire axis corresponds to the easy (hard) axis of the nanowires arrays, resulting in higher (lower) remanences and coercivities. The opposite is the case for the $Fe_{0.51}Ni_{0.49}$ and $Fe_{0.80}Ni_{0.20}$ NWs. As has been previously discussed in the literature [18], [49], [50], [51], this change in easy axis can be understood as the interplay between the shape anisotropy and the magnetostatic interactions among nanowires in the array. If the magnetocrystalline and magnetoelastic anisotropies can be neglected, then the arrays of NWs for which the shape anisotropy is significantly higher than the magnetostatic interactions (both measured as energy densities) will have the easy axis along the nanowire axis. On the other hand, when the magnetostatic energy density is close to or larger than the shape anisotropy, the resulting weakening of the shape anisotropy leads to a swap between the easy and hard axis directions, with the nanowire axis ending as the hard axis.

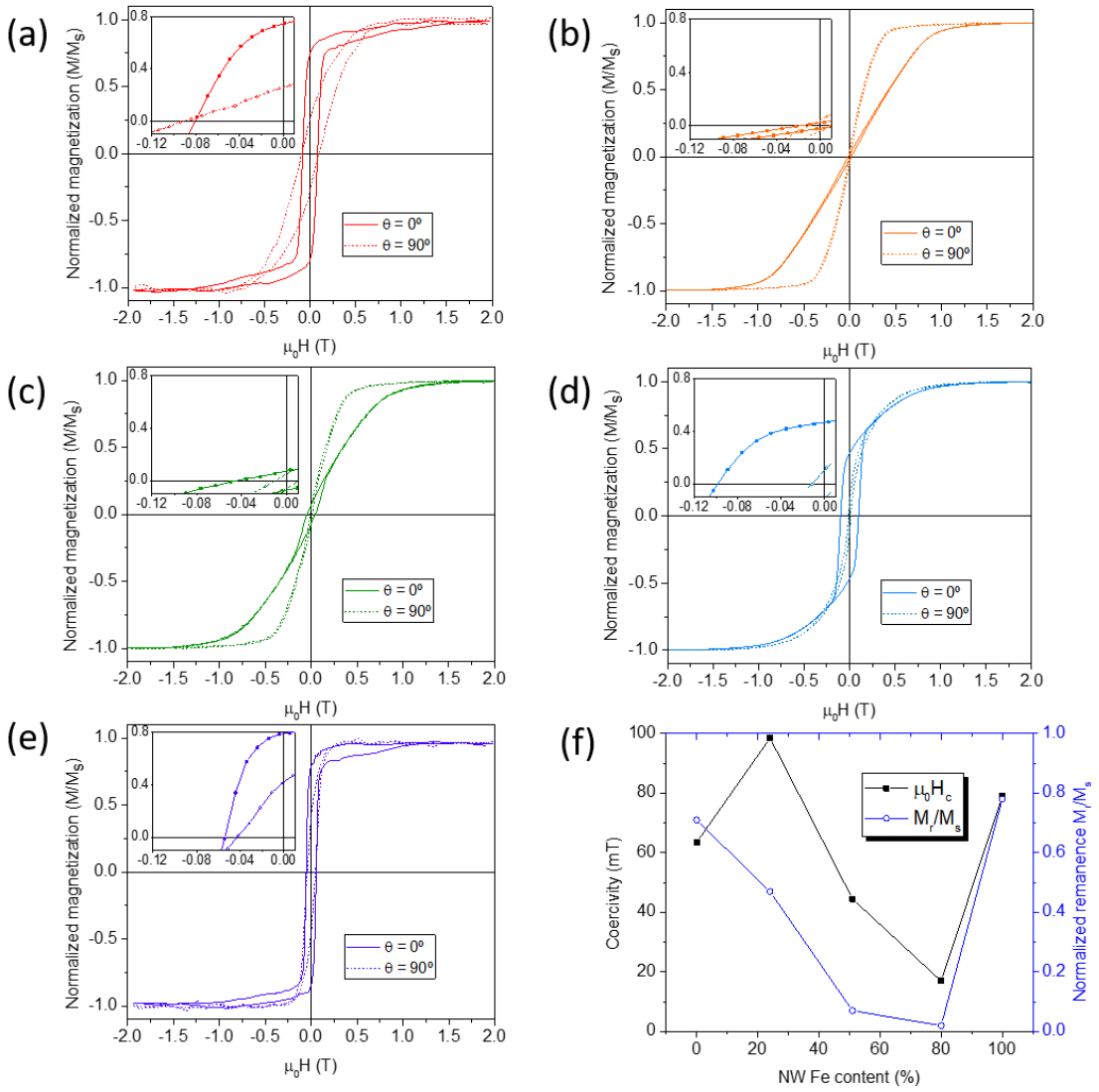

Figure 4. *Room temperature VSM hysteresis loops measured for arrays of NWs with compositions with the magnetic field applied with an angle θ = 0° and 90° (parallel and perpendicular to the NW axis, respectively): (a) Fe, (b) $Fe_{0.80}Ni_{0.20}$, (c) $Fe_{0.51}Ni_{0.49}$, (d) $Fe_{0.24}Ni_{0.76}$ and (e) Ni; and (f) evolution of the coercivity and normalized remanence of the arrays of NWs with chemical composition for θ = 0°. Insets in each subfigure show the second quadrant of each hysteresis loop.*

Thus, the correlation between the coercivity of the arrays of nanowires and their chemical composition might be explained due to the different values of the shape anisotropy and the magnetostatic interactions between the samples. In order to estimate both the shape anisotropy and magnetostatic interactions between the NWs, as well as identify the magnetization reversal mechanism, coercivity angular measurements were carried out and analysed.

3.3.1 Magnetization reversal study

A study of the evolution of the coercivity with the angle at which the external field is applied in relation to the NWs longitudinal axis was carried out, as this can support the identification of the magnetization reversal mechanism. The magnetization reversal modes considered were coherent rotation, transverse domain wall and vortex domain wall (curling).

For both the coherent rotation and transverse wall modes, the coercivity is given by

$$H_c^x(\theta) = \frac{2\,K_t(x)\sqrt{1-t^2+t^4}}{\mu_0 M_S^2(1+t^2)} M_s \tag{2}$$

where x represents either the coherent or transverse cases, $t = \tan(\theta)^{1/3}$ and $K_t(x)$ is the total magnetic anisotropy. On the other hand, the angle-dependent coercivity of a NW with the curling magnetization reversal mode can be modelled as

$$H_c(\theta) = 2\pi M_s \left| \frac{(2N_z - {}^{k}/_{S^2})(2N_x - {}^{k}/_{S^2})}{\sqrt{(2N_z - {}^{k}/_{S^2})^2 \sin^2\theta + (2N_x - {}^{k}/_{S^2})^2 \cos^2\theta}} \right| \tag{3}$$

where $S = r/r_0$, r the NW radius, $r_0 = A^{1/2}/M_s$ and $k = q^2/\pi$ (q is the smallest solution of the Bessel functions and is 1.8412 for a cylinder).

An in-depth discussion on these models and how to analyse the data extracted from the angular coercivity measurements can be found in the Supplementary Material. Such an analysis can yield estimates for the total and shape anisotropy constants (K_t and K_{sh}, respectively), and therefore of the non-shape anisotropy $K_t - K_{sh}$.

The model fits of the samples studied all yielded transverse domain wall as the dominant reversal mechanism in the array of NWs (see Fig. 5), as it had the lowest coercivity values of the three models considered. This is consistent with previous results in the literature for Co, Ni, CoNi and CoFe NWs [30], [37], [52], [53] showing that single-segment NWs with high aspect ratio have magnetization reversal driven by the transverse domain wall mechanism, due to the higher energy cost of the curling and coherent reversal modes. Other magnetization reversal modes, such as the curling mode [54], [55], typically require NWs with larger diameters and/or shorter lengths. Note that another version of Fig. 5, with each subfigure zoomed-in as needed to be able to visually appreciate the changes in coercivity, is available in the Supplementary Material.

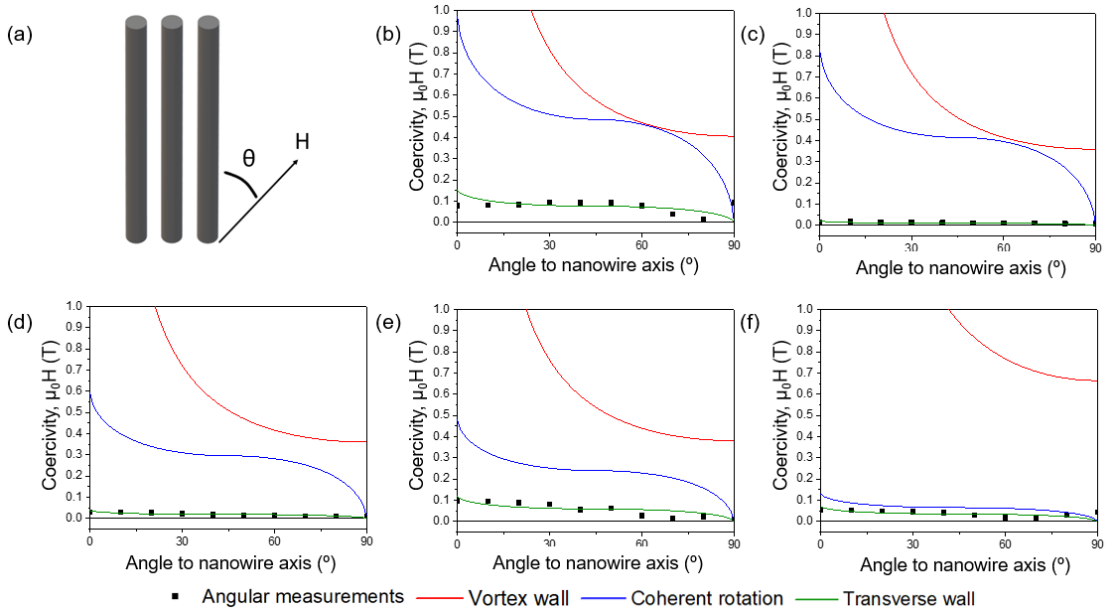

Figure 5. *(a) Diagram sketching the angular measurements performed and (b)-(f) coercivity measured at different angles to the NWs axis and fits to magnetization reversal models for the arrays of NWs with the following composition: (b) Fe, (c) $Fe_{0.80}Ni_{0.20}$, (d) $Fe_{0.51}Ni_{0.49}$, (e) $Fe_{0.24}Ni_{0.76}$, and (f) Ni.*

The non-shape magnetic anisotropy (Table 1) showed a range of values, with the pure reference Ni sample having the lowest absolute value, and the $Fe_{0.80}Ni_{0.20}$ sample having the largest one. The negative sign shows that this anisotropy works against the main magnetic hardening factor, namely the shape anisotropy K_{sh}, and tends to ease the magnetization reversal. Note that (as discussed in the Supplementary Material) in the transverse domain wall case, K_{sh} is calculated as a function of sample magnetization saturation M_s and its estimated transverse domain wall width.

It is observed that the samples with an easy axis along the NW axis (Fig. 4) have shape anisotropies that are between 50 and 100% larger than their non-shape anisotropies. On the other hand, samples with the hard axis at $\theta = 0°$ have shape anisotropies only 10-20% higher than the non-shape anisotropies. If the non-shape anisotropy values can be attributed to magnetostatic interactions, then these values for the samples studied are in line with the theory and experimental results previously discussed in the literature [18], [49], [50], [51]. However, since the non-shape anisotropy includes contributions from the magnetostatic interactions and the magnetocrystalline anisotropy, first order reversal curve (FORC) measurements were performed to study the evolution of the magnetic interactions across the samples to be able to separate both contributions.

Table 1. *Evolution of the saturation magnetization and non-shape magnetic anisotropy with sample composition.*

Composition	**M_s (A m^2 kg^{-1})** [47]	**K_{sh} (10^3 J m^{-3})**	**$K_t - K_{sh}$ (10^3 J m^{-3})**
Fe	222	240	-110
$Fe_{0.80}Ni_{0.20}$	218	240	-220
$Fe_{0.51}Ni_{0.49}$	163	200	-170
$Fe_{0.24}Ni_{0.76}$	112	120	-60
Ni	58	30	-20

3.3.2 First-Order Reversal Curve analysis

First Order Reversal Curve (FORC) analysis has been carried out to study the role of the magnetic interactions in the arrays of FeNi NWs. In FORC measurements, the sample is saturated at a certain saturation field, H_{sat}, and then minor hysteresis loop branches are taken from a given reversal field, H_r, up to a maximum field, H_{max}. Once a minor hysteresis loop is measured, the sample is saturated again and H_r is decreased slightly while H_{max} is increased, so that each minor hysteresis loop covers a slightly longer range than the previous one. The procedure is completed until the last minor hysteresis loop is measured, which covers the range of a full hysteresis loop (Fig. 6 (a)).

Then, the FORC intensity distribution ρ_{FORC}, calculated from the magnetization M at each measurement point, is given by

$$\rho_{FORC} = \frac{1}{2}\frac{\partial^2 M}{\partial H\, \partial H_r}, H > H_r \quad (4)$$

With H_r being the reversal field for the minor hysteresis loop of the measurement point and H being the applied field at the measurement point. The discrete ρ_{FORC} values thus obtained were then processed using the utility package FORCinel [42] to produce a continuous FORC distribution, with the data being typically represented in terms of the coercive and interaction fields (H_c and H_u, respectively), which are given by

$$H_c = \frac{H - H_r}{2}, \; H_u = -\frac{H + H_r}{2} \quad (5)$$

FORC measurements were taken setting a saturation field of $\mu_0 H_{sat}$ = 1.5 T, with a maximum coercivity $\mu_0 H_c$ of 0.5 T, and values of $\mu_0 H_{u,\,min}$ = -0.2 T and $\mu_0 H_{u,\,max}$ = 0.2 T. Typical FORC curves measured in this manner can be seen in Fig. 6 (a)).

The FORC diagrams of the arrays of NWs with different composition can be found in Fig. 6. The $Fe_{0.80}Ni_{0.20}$ sample showed the typical T-shape behaviour (with a long intensity distribution along the H_u interactions axis) of interacting magnetic NWs [55], [56], [57], [58], [59], [60], with the NWs having an interaction field $\mu_0 \Delta H_u$ of around 82 mT. ΔH_u represents the maximum interaction field between the NWs and is estimated as the half-width at half-maximum of the FORC distribution parallel to the H_u axis [35].

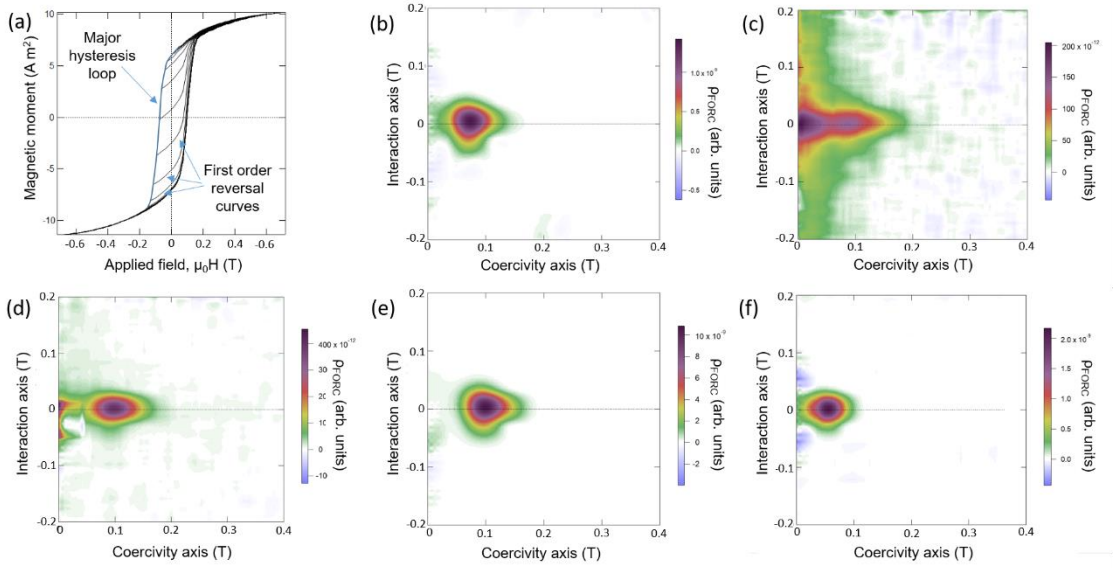

Figure 6. *(a) Representative example of FORC measurements ($Fe_{0.24}Ni_{0.76}$ sample), and (b)-(f) FORC diagrams measured for the samples with the following composition: (b) Fe, (c) $Fe_{0.80}Ni_{0.20}$, (d) $Fe_{0.51}Ni_{0.49}$, (e) $Fe_{0.24}Ni_{0.76}$, and (f) Ni.*

The other four samples show a very narrow FORC distribution along the H_u axis. The diagram obtained for the Fe and $Fe_{0.24}Ni_{0.76}$ samples resemble the "wishbone" shape observed for low-interactions systems [56], [60], [61], [62], although with a highly deformed shape. Instead, the shape of the spots is very similar to the results for a magnetic recording device [61]. The discussion and simulations for Ni nanopillar arrays in [61] also indicate that the cause for this shape lies in the combination of a wide nanowire coercivity distribution and very low interactions between them. For progressively higher interactions, the wishbone and then T-shape appear. However, if the coercivity range remains significant, the wishbone shape might not appear even on increasing interactions. This can be seen in Fig. 6 (d), where there is a wider distribution along

both the H_u and H_c axis, in particular with the existence of a secondary low-H_c spot centred on the H_c axis. The small negative-value ridge found around $\mu_0 H_c = 0$ mT and $\mu_0 H_u = 100$ mT in Fig. 6 (c) and 6 (e), and especially Fig. 6 (d), is a consequence of the coupling of the reversible and irreversible components of magnetic reversal [61]. Additionally, the calculation of the FORC marginal coercivity distributions was done by determining the peaks in the plotted FORC distribution along the coercivity axis in the FORC diagram. The results (see Fig. 3 in the Supplementary Material) show agreement between the maximum of the marginal distributions and the corresponding coercivities extracted from the hysteresis loops for all samples except for the $Fe_{0.51}Ni_{0.49}$ sample. For this sample, two distinct maxima can be found in the coercivity marginal distribution, one at very close to the intersection between axis and another one around 95 mT, compared to the coercivity obtained from the hysteresis loop (45 mT). Taking into account how the non-shape magnetic anisotropy acts as a weakening mechanism of the shape anisotropy, this indicates that the $Fe_{0.51}Ni_{0.49}$ sample contains nanowires affected by a high local non-shape anisotropy (corresponding to the maximum at low-coercivity) and nanowires with a low local non-shape anisotropy (corresponding to the peak in the diagram at higher coercivity). Given that the non-shape anisotropy is dominated by the magnetostatic anisotropy (see below), the maxima at higher coercivity would then correspond to magnetically isolated nanowires which therefore experience low magnetic interactions.

In comparison with the values obtained for the non-shape magnetic anisotropies using the coercivity angular measurements, it can be seen that the samples with the smallest absolute values (arrays of NWs with the composition of Fe, $Fe_{0.24}Ni_{0.76}$, and Ni) had the smallest magnetic interactions as observed through FORC measurements, while the $Fe_{0.51}Ni_{0.49}$ sample showed an intermediate level of interactions in FORC diagram and the second largest absolute value for $K_t - K_{sh}$. The $Fe_{0.80}Ni_{0.20}$ sample had the strongest interactions and the largest value of $K_t - K_{sh}$. The difference between the coercivities of the Fe and $Fe_{0.80}Ni_{0.20}$ samples observed in Fig. 4 therefore seems to stem mainly from a difference in magnetostatic interactions between the NWs, not in their magnetocrystalline anisotropies. Thus, these results show that the evolution with the chemical composition of the non-shape magnetic anisotropy is in line with the evolution of the magnetic interactions, indicating that $K_t - K_{sh}$ is dominated by those magnetostatic interactions, with the contribution of the magnetocrystalline anisotropy to the non-shape anisotropy being negligible in comparison. The magnetostatic interactions are thus seen to act as a magnetization reversal weakening mechanism. Considering this, together with the discussion at the end of the previous section, it can be concluded that the changes in remanence and coercivity observed between the samples in Fig. 4 are due to changes in the easy axis direction from $\theta = 0°$ (where the shape anisotropy dominates) to $\theta = 90°$ (where the magnetostatic interactions dominate) depending on the chemical composition of the NWs.

4. Conclusions

The electrochemical synthesis of magnetic FeNi NWs showed the anomalous co-deposition of Fe, which was observed as the electrodeposition potential and electrolyte composition were modified. The change in Fe selectivity and the anomalous co-deposition potential range were explained in terms of the differing adsorption stability of $FeOH^+$ and $NiOH^+$ ions within a modified Bocris-Drazic-Despic (BDD) model. These results highlight the importance of the understanding and application of electrochemical theory for the analysis of FeNi NWs, as well as paves the way for the future prediction of anomalous co-deposition trends in other works around electrodeposited FeNi. Additionally, X-ray diffraction measurements showed a mixture of bcc and fcc crystalline phases with varying the NWs composition.

The magnetic characterization of the main samples studied showed a wide range of coercivity values, from 20 mT for the $Fe_{0.80}Ni_{0.20}$ sample to 100 mT for the $Fe_{0.24}Ni_{0.76}$ sample. To further analyse the magnetic properties of the arrays of FeNi NWs, angular coercivity measurements were performed, to study the magnetization reversal mechanisms of the arrays of NWs and their magnetic anisotropies. All samples were found to preferably reverse their magnetization through the transverse domain wall mechanism, with the non-shape anisotropies contributing as magnetization reversal weakening factors. FORC analysis was then used to show that the values of the non-shape anisotropies of the samples were correlated with the magnetic interactions among the NWs in the arrays. This indicated that the non-shape magnetic anisotropy is dominated by magnetostatic interactions that facilitate magnetization reversal.

The combination of hysteresis loops, angular coercivity and FORC measurements and their combined analysis explained how the changes in the chemical composition of the NWs lead to changes in the magnetostatic interactions between them and how this causes a change in the easy axis preference when the value of the magnetostatic anisotropy is close to that of the shape anisotropy. Thus, this work shows the potential of the FeNi NWs system as a platform from which to easily develop different applications (from magnetic information storage devices to magnetic sensors), thanks to the wide range of coercivity, magnetization saturation and magnetic interactions strength that can be achieved by simply tuning the parameters involved in the electrochemical synthesis of such nanostructures. The analysis done in this work, both concerning Fe anomalous co-deposition as well as the magnetic properties of the NWs and the correlation with their morphology, composition, and structure, constitutes key information for further precisely controlling the magnetic properties of the NWs for their development and implementation in different technological applications.

Acknowledgments

Authors acknowledge financial support through the collaboration project between Robert Bosch GmbH and IMDEA Nanociencia. Authors acknowledge support from MICINN-AEI through the projects *NEXUS* (PID2020-115215RB-C21), *COSMAG* (PCI2020-112143, M-era.Net Programme) and the ‘‘Severo Ochoa’’ Programme for Centers of Excellence in R&D (CEX2020-001039-S), and by the Regional Government of Madrid through *NANOMAGCOST* project (S2018/NMT-4321). A.J.C.-H. acknowledges support from “La Caixa” Foundation (ID 100010434) through the Doctoral INPhINIT Incoming programme (LCF/BQ/DI20/1178002). E.M.P. acknowledges support from AEI through the Juan de la Cierva – Incorporación program (grant IJC2020-043011-I/MCIN/AEI/10.13039/501100011033) and EU by NextGenerationEU/PRTR.

References

[1] Y. P. Ivanov, A. Chuvilin, S. Lopatin, and J. Kosel, ‘Modulated magnetic nanowires for controlling domain wall motion: toward 3D magnetic memories’, *ACS Nano*, vol. 10, no. 5, pp. 5326–5332, 2016, doi: 10.1021/acsnano.6b01337.

[2] G. Hrkac, J. Dean, and D. A. Allwood, ‘Nanowire spintronics for storage class memories and logic’, *Philos. Trans. R. Soc. Math. Phys. Eng. Sci.*, vol. 369, no. 1948, pp. 3214–3228, 2011, doi: 10.1098/rsta.2011.0138.

[3] J. Um *et al.*, ‘Fabrication of long-range ordered Aluminum oxide and Fe/Au multilayered nanowires for 3-D magnetic memory’, *IEEE Trans. Magn.*, vol. 56, no. 2, pp. 1–6, 2020, doi: 10.1109/TMAG.2019.2942946.

[4] J. A. Moreno, C. Bran, M. Vazquez, and J. Kosel, ‘Cylindrical magnetic nanowires applications’, *IEEE Trans. Magn.*, vol. 57, no. 4, pp. 1–17, 2021, doi: 10.1109/TMAG.2021.3055338.

[5] X. Chen, C. K. Y. Wong, C. A. Yuan, and G. Zhang, ‘Nanowire-based gas sensors’, *Sens. Actuators B Chem.*, vol. 177, pp. 178–195, 2013, doi: 10.1016/j.snb.2012.10.134.

[6] N. S. Ramgir, Y. Yang, and M. Zacharias, ‘Nanowire-based Sensors’, *Small*, vol. 6, no. 16, pp. 1705–1722, 2010, doi: 10.1002/smll.201000972.

[7] J. Dong, L. Ren, Y. Zhang, X. Cui, P. Hu, and J. Xu, ‘Direct electrodeposition of cable-like CuO@Cu nanowires array for non-enzymatic sensing’, *Talanta*, vol. 132, pp. 719–726, 2015, doi: 10.1016/j.talanta.2014.10.027.

[8] J. Meng and Z. Li, ‘Schottky-contacted nanowire sensors’, *Adv. Mater.*, vol. 32, no. 28, p. 2000130, 2020, doi: 10.1002/adma.202000130.

[9] C. García Núñez, F. Liu, W. T. Navaraj, A. Christou, D. Shakthivel, and R. Dahiya, ‘Heterogeneous integration of contact-printed semiconductor nanowires for high-performance devices on large areas’, *Microsyst. Nanoeng.*, vol. 4, no. 1, p. 22, 2018, doi: 10.1038/s41378-018-0021-6.

[10] C. Yang *et al.*, ‘Silver nanowires: from scalable synthesis to recyclable foldable electronics’, *Adv. Mater.*, vol. 23, no. 27, pp. 3052–3056, Jul. 2011, doi: 10.1002/adma.201100530.

[11] S. Lee *et al.*, ‘Ag nanowire reinforced highly stretchable conductive fibers for wearable Electronics’, *Adv. Funct. Mater.*, vol. 25, no. 21, pp. 3114–3121, 2015, doi: 10.1002/adfm.201500628.

[12] J.-L. Wang, M. Hassan, J.-W. Liu, and S.-H. Yu, ‘Nanowire assemblies for flexible electronic devices: recent advances and perspectives’, *Adv. Mater.*, vol. 30, no. 48, p. 1803430, 2018, doi: 10.1002/adma.201803430.

[13] W. Li, H. Zhang, S. Kagita, and A. Shamim, 'All screen-printed, polymer-nanowire based foldable electronics for mm-wave applications', *Adv. Mater. Technol.*, vol. 6, no. 11, p. 2100525, 2021, doi: 10.1002/admt.202100525.
[14] C. Fernández-González *et al.*, 'Asymmetrical magnetization processes induced by compositional gradients in ferromagnetic nanowires', *Scr. Mater.*, vol. 243, p. 115970, 2024, doi: 10.1016/j.scriptamat.2024.115970.
[15] S. Ruiz-Gómez *et al.*, 'Observation of a topologically protected state in a magnetic domain wall stabilized by a ferromagnetic chemical barrier', *Sci. Rep.*, vol. 8, no. 1, p. 16695, 2018, doi: 10.1038/s41598-018-35039-6.
[16] M. Méndez, V. Vega, S. González, R. Caballero-Flores, J. García, and V. M. Prida, 'Effect of sharp diameter geometrical modulation on the magnetization reversal of bi-segmented FeNi nanowires', *Nanomaterials*, vol. 8, no. 8, 2018, doi: 10.3390/nano8080595.
[17] C. Fernández-González *et al.*, 'Electrodeposited magnetic nanowires with radial modulation of composition', *Nanomaterials*, vol. 12, no. 15, 2022, doi: 10.3390/nano12152565.
[18] N. Mansouri *et al.*, 'Electrodeposition of equiatomic FeNi and FeCo nanowires: Structural and magnetic properties', *J. Magn. Magn. Mater.*, vol. 493, p. 165746, 2020, doi: https://doi.org/10.1016/j.jmmm.2019.165746.
[19] Á. Llavona, L. Pérez, M. C. Sánchez, and V. de Manuel, 'Enhancement of anomalous codeposition in the synthesis of Fe–Ni alloys in nanopores', *Electrochimica Acta*, vol. 106, pp. 392–397, 2013, doi: https://doi.org/10.1016/j.electacta.2013.05.116.
[20] X. Zhang, H. Zhang, T. Wu, Z. Li, Z. Zhang, and H. Sun, 'Comparative study in fabrication and magnetic properties of FeNi alloy nanowires and nanotubes', *J. Magn. Magn. Mater.*, vol. 331, pp. 162–167, 2013, doi: https://doi.org/10.1016/j.jmmm.2012.11.033.
[21] K. V. Frolov *et al.*, 'Structural and magnetic properties of Ni-Fe nanowires in the pores of polymer track membranes', *J. Magn. Magn. Mater.*, vol. 489, p. 165415, 2019, doi: https://doi.org/10.1016/j.jmmm.2019.165415.
[22] Q. Liu, J. Wang, Z. Yan, and D. Xue, 'Characterization and magnetic properties of $Fe_{1-x}Ni_x$ nanowire arrays', *Phys. Rev. B*, vol. 72, no. 14, p. 144412, 2005, doi: 10.1103/PhysRevB.72.144412.
[23] F. Meneses, A. Pedernera, C. Blanco, N. Bajales, S. E. Urreta, and P. G. Bercoff, '$L1_0$-FeNi ordered phase in AC electrodeposited iron-nickel biphasic nanowires', *J. Alloys Compd.*, vol. 766, pp. 373–381, 2018, doi: 10.1016/j.jallcom.2018.06.307.
[24] M. S. Salem, P. Sergelius, R. Zierold, J. M. Montero Moreno, D. Görlitz, and K. Nielsch, 'Magnetic characterization of nickel-rich NiFe nanowires grown by pulsed electrodeposition', *J Mater Chem*, vol. 22, no. 17, pp. 8549–8557, 2012, doi: 10.1039/C2JM16339J.
[25] A. Pierrot *et al.*, 'Switching field distribution of ultradense arrays of single-crystalline magnetic nanowires', *Appl. Phys. Lett.*, vol. 122, no. 26, p. 262403, 2023, doi: 10.1063/5.0148774.
[26] C. Bran *et al.*, 'Correlation between structure and magnetic properties in Co_xFe_{100-x} nanowires: the roles of composition and wire diameter', *J. Phys. Appl. Phys.*, vol. 48, no. 14, Art. no. 14, 2015, doi: 10.1088/0022-3727/48/14/145304.
[27] E. M. Palmero, C. Bran, R. P. del Real, C. Magén, and M. Vázquez, 'Magnetic behavior of NiCu nanowire arrays: Compositional, geometry and temperature dependence', *J. Appl. Phys.*, vol. 116, no. 3, p. 033908, 2014, doi: 10.1063/1.4890358.
[28] E. Yoo *et al.*, 'Composition-driven crystal structure transformation and magnetic properties of electrodeposited Co–W alloy nanowires', *J. Alloys Compd.*, vol. 843, p. 155902, 2020, doi: 10.1016/j.jallcom.2020.155902.
[29] A. S. Samardak *et al.*, 'Variation of magnetic anisotropy and temperature-dependent FORC probing of compositionally tuned Co-Ni alloy nanowires', *J. Alloys Compd.*, vol. 732, pp. 683–693, 2018, doi: 10.1016/j.jallcom.2017.10.258.
[30] C. Bran, A. P. Espejo, E. M. Palmero, J. Escrig, and M. Vázquez, 'Angular dependence of coercivity with temperature in Co-based nanowires', *J. Magn. Magn. Mater.*, vol. 396, pp. 327–332, 2015, doi: 10.1016/j.jmmm.2015.08.056.

[31] C. Bran, E. M. Palmero, R. P. del Real, and M. Vazquez, 'CoFeCu electroplated nanowire arrays: Role of composition and annealing on structure and magnetic properties', *Phys. Status Solidi A*, vol. 211, no. 5, pp. 1076–1082, 2014, doi: 10.1002/pssa.201300766.
[32] S. L. Viñas *et al.*, 'Magnetic hardening of $Fe_{30}Co_{70}$ nanowires', *Nanotechnology*, vol. 26, no. 41, p. 415704, 2015, doi: 10.1088/0957-4484/26/41/415704.
[33] C. Bran *et al.*, 'Magnetization ratchet in cylindrical nanowires', *ACS Nano*, vol. 12, no. 6, pp. 5932–5939, 2018, doi: 10.1021/acsnano.8b02153.
[34] C. Bran *et al.*, 'Spin configuration of cylindrical bamboo-like magnetic nanowires', *J. Mater. Chem. C*, vol. 4, no. 5, Art. no. 5, 2016, doi: 10.1039/C5TC04194E.
[35] E. M. Palmero, C. Bran, R. P. del Real, and M. Vázquez, 'Vortex domain wall propagation in periodically modulated diameter FeCoCu nanowire as determined by the magneto-optical Kerr effect', *Nanotechnology*, vol. 26, no. 46, Art. no. 46, 2015, doi: 10.1088/0957-4484/26/46/461001.
[36] E. M. Palmero *et al.*, 'Stepwise magnetization reversal of geometrically tuned in diameter Ni and FeCo bi-segmented nanowire arrays', *Nano Res.*, vol. 12, no. 7, pp. 1547–1553, 2019, doi: 10.1007/s12274-019-2385-9.
[37] L. G. Vivas *et al.*, 'Magnetic anisotropy in CoNi nanowire arrays: Analytical calculations and experiments', *Phys Rev B*, vol. 85, no. 3, p. 035439, 2012, doi: 10.1103/PhysRevB.85.035439.
[38] O. Dragos, H. Chiriac, N. Lupu, M. Grigoras, and I. Tabakovic, 'Anomalous codeposition of *fcc* NiFe nanowires with 5–55% Fe and their morphology, crystal structure and magnetic properties', *J. Electrochem. Soc.*, vol. 163, no. 3, pp. D83–D94, 2015, doi: 10.1149/2.0771603jes.
[39] H. Masuda and K. Fukuda, 'Ordered metal nanohole arrays made by a two-step replication of honeycomb structures of anodic alumina', *Science*, vol. 268, no. 5216, pp. 1466–1468, 1995, doi: 10.1126/science.268.5216.1466.
[40] B. Yoo, Y. Rheem, W. P. Beyermann, and N. V. Myung, 'Magnetically assembled 30 nm diameter nickel nanowire with ferromagnetic electrodes', *Nanotechnology*, vol. 17, no. 10, p. 2512, 2006, doi: 10.1088/0957-4484/17/10/012.
[41] Xinsheng Peng and Aicheng Chen, 'Electrochemical fabrication of novel nanostructures based on anodic alumina', *Nanotechnology*, vol. 15, no. 7, p. 743, 2004, doi: 10.1088/0957-4484/15/7/005.
[42] R. J. Harrison and J. M. Feinberg, 'FORCinel: An improved algorithm for calculating first-order reversal curve distributions using locally weighted regression smoothing', *Geochem. Geophys. Geosystems*, vol. 9, no. 5, 2008, doi: 10.1029/2008GC001987.
[43] S. Hessami and C. W. Tobias, 'A mathematical model for anomalous codeposition of nickel-iron on a rotating disk electrode', *J. Electrochem. Soc.*, vol. 136, no. 12, pp. 3611–3616, 1989, doi: 10.1149/1.2096519.
[44] A. J. Bard and L. R. Faulkner, *Electrochemical Methods: Fundamentals and Applications*, 2nd Edition. Wiley, 2001.
[45] A. Ramazani, V. Asgari, A. H. Montazer, and M. A. Kashi, 'Tuning magnetic fingerprints of FeNi nanowire arrays by varying length and diameter', *Curr. Appl. Phys.*, vol. 15, no. 7, pp. 819–828, 2015, doi: https://doi.org/10.1016/j.cap.2015.04.023.
[46] J. M. Baik, M. Schierhorn, and M. Moskovits, 'Fe nanowires in nanoporous alumina: Geometric effect versus influence of pore walls', *J. Phys. Chem. C*, vol. 112, no. 7, pp. 2252–2255, 2008, doi: 10.1021/jp711621v.
[47] Okamoto, H., *Phase diagrams of binary iron alloys*. Materials Park, Ohio, USA: The Materials Information Society.
[48] D. L. Zagorskiy, S. V. Semenov, S. V. Komogortsev, D. A. Balaev, I. M. Doludenko, and L. V. Panina, 'Magnetization processes in two-dimensional arrays of iron nanowires', *J. Magn. Magn. Mater.*, vol. 595, p. 171573, 2024, doi: 10.1016/j.jmmm.2023.171573.
[49] M. Staňo and O. Fruchart, 'Chapter 3 - Magnetic Nanowires and Nanotubes', in *Handbook of Magnetic Materials*, vol. 27, E. Brück, Ed., Elsevier, 2018, pp. 155–267. doi: 10.1016/bs.hmm.2018.08.002.

[50] A. Encinas-Oropesa, M. Demand, L. Piraux, I. Huynen, and U. Ebels, ‘Dipolar interactions in arrays of nickel nanowires studied by ferromagnetic resonance’, *Phys. Rev. B*, vol. 63, no. 10, p. 104415, 2001, doi: 10.1103/PhysRevB.63.104415.
[51] M. Vázquez, K. Pirota, J. Torrejón, D. Navas, and M. Hernández-Vélez, ‘Magnetic behaviour of densely packed hexagonal arrays of Ni nanowires: Influence of geometric characteristics’, *NANO2004*, vol. 294, no. 2, pp. 174–181, 2005, doi: 10.1016/j.jmmm.2005.03.032.
[52] R. Lavín, J. C. Denardin, J. Escrig, D. Altbir, A. Cortés, and H. Gómez, ‘Angular dependence of magnetic properties in Ni nanowire arrays’, *J. Appl. Phys.*, vol. 106, no. 10, p. 103903, 2009, doi: 10.1063/1.3257242.
[53] M. Vázquez and L. G. Vivas, ‘Magnetization reversal in Co-base nanowire arrays’, *Phys. Status Solidi B*, vol. 248, no. 10, pp. 2368–2381, Oct. 2011, doi: 10.1002/pssb.201147092.
[54] J. Almeira, F. Meneses, J. Milano, C. Ramos, S. E. Urreta, and P. G. Bercoff, ‘Effective anisotropy in Fe-Ni nanowire arrays with strong dipolar interaction’, *J. Magn. Magn. Mater.*, vol. 580, p. 170929, Aug. 2023, doi: 10.1016/j.jmmm.2023.170929.
[55] M. Alikhani, A. Ramazani, M. Almasi Kashi, S. Samanifar, and A. H. Montazer, ‘Irreversible evolution of angular-dependent coercivity in $Fe_{80}Ni_{20}$ nanowire arrays: Detection of a single vortex state’, *J. Magn. Magn. Mater.*, vol. 414, pp. 158–167, 2016, doi: 10.1016/j.jmmm.2016.04.035.
[56] E. M. Palmero, F. Béron, C. Bran, R. P. del Real, and M. Vázquez, ‘Magnetic interactions in compositionally modulated nanowire arrays’, *Nanotechnology*, vol. 27, no. 43, p. 435705, 2016, doi: 10.1088/0957-4484/27/43/435705.
[57] M. Varga *et al.*, ‘FORC and TFORC analysis of electrodeposited magnetic shape memory nanowires array’, *J. Alloys Compd.*, vol. 897, p. 163211, 2022, doi: 10.1016/j.jallcom.2021.163211.
[58] M. Ciureanu *et al.*, ‘First Order Reversal Curves (FORC) diagrams of Co nanowire arrays’, *J. Nanosci. Nanotechnol.*, vol. 8, no. 11, pp. 5725–5732, 2008, doi: 10.1166/jnn.2008.228.
[59] A. H. A. Elmekawy *et al.*, ‘Magnetic properties and FORC analysis of iron nanowire arrays’, *Mater. Today Commun.*, vol. 25, p. 101609, 2020, doi: 10.1016/j.mtcomm.2020.101609.
[60] F. Béron, L. Clime, M. Ciureanu, D. Ménard, R. W. Cochrane, and A. Yelon, ‘Magnetostatic interactions and coercivities of ferromagnetic soft nanowires in uniform length arrays’, *J. Nanosci. Nanotechnol.*, vol. 8, no. 6, pp. 2944–2954, 2008, doi: 10.1166/jnn.2008.159.
[61] C. R. Pike, C. A. Ross, R. T. Scalettar, and G. Zimanyi, ‘First-order reversal curve diagram analysis of a perpendicular nickel nanopillar array’, *Phys Rev B*, vol. 71, no. 13, p. 134407, 2005, doi: 10.1103/PhysRevB.71.134407.
[62] F. Béron, L. A. S. de Oliveira, M. Knobel, and K. R. Pirota, ‘A novel method for identifying the local magnetic viscosity process of heterogeneous magnetic nanostructures’, *J. Phys. Appl. Phys.*, vol. 46, no. 4, p. 045003, 2012, doi: 10.1088/0022-3727/46/4/045003.